

# PERFORMANCES OF POLARIMETRIC SUBSPACE SAR PROCESSORS FOR TARGET DETECTION AND INTERFERENCE REJECTION

*F. Brigui<sup>1</sup>, G. Ginolhac<sup>3</sup>, L. Thirion-Lefevre<sup>2</sup> and P. Forster<sup>3</sup>*

<sup>1</sup> University of Toulouse  
ISAE/DEOS  
1 place Emile Blouin  
31500 Toulouse  
France

<sup>2</sup> SONDR  
Supelec  
3 rue Joliot-Curie  
91192 Gif-sur-Yvette  
France

<sup>3</sup> SATIE  
UniverSud  
61 av du Président Wilson  
94235 CACHAN  
France

## ABSTRACT

We develop a new Synthetic Aperture Radar (SAR) algorithm based on physical models for the detection of a Man-Made Target (MMT) embedded in strong interferences. These physical models for the MMT and the interferences are integrated in low-dimension subspaces. Our SAR algorithm consists of applying the oblique projection of the received signal into the target subspace along the interference one. We apply our algorithms to FoPen (Foliage Penetration) detection. Its performances are better compared to those obtained with previous SAR algorithms: the MMT detection is highly improved and the interferences are strongly rejected. We also study the robustness of our new SAR algorithm to interference modeling errors. Finally, we present results on real data.

**Index Terms**— SAR processors, Subspace models, Oblique projection, Statistical performances, FoPen.

## 1. INTRODUCTION

Detection of target in strong disturbance using Synthetic Aperture Radar (SAR) is a current issue in the signal processing community. More precisely, for FoPen (Foliage Penetration) application, we want to detect a Man-Made Target (MMT) located in a forest. In this forest environment, the disturbance could be considered as the sum of deterministic interferences caused by the trunks of trees and a random noise caused by the foliage, the branches of the trees, . . . . By using classical SAR images [1], MMT detection is almost impossible because a lot of false alarms remain.

We have proposed in previous works to reconsider the SAR algorithms by including prior-knowledge based on simple physical models of the MMT and the interferences. In the first algorithm [2], the Signal Subspace Detector SAR (SSDSAR), a MMT is assumed to be a set of plates whose scattering belongs to a low-dimension subspace. The SSDSAR consists of projecting orthogonally the SAR received signal into the plate subspace. Compared to classical SAR processors, the SSDSAR algorithm has shown a  $5\text{dB}$  detection gain for single polarization [2] and a  $8\text{dB}$  detection gain for double polarization (HH and VV) [3]. Therefore, the SSDSAR allows to increase

MMT detection in random noise; nevertheless, false alarms due to the interferences remain high.

To reduce false alarms due to the interferences, another SAR algorithm (SISDSAR for Signal and Interference Subspace Detector SAR) has been proposed in [4]. The interferences are assumed to be dielectric cylinders whose scattering also belongs to a low-dimension subspace. The SISDSAR consists of the difference of the orthogonal projection of the received signal into the target subspace with the orthogonal projection of the received signal into the interference subspace. Unfortunately, the SISDSAR may perform poorly: the interference responses are widely decreased but the response of the target may also be reduced.

We propose in this paper to develop a new SAR algorithm (OBSAR for Oblique SAR) [5] in order to reduce false alarms due to the interferences without degrading the MMT detection. As for the SSDSAR and the SISDSAR, prior knowledge about MMT and interferences (trunks of trees) are integrated in two low-dimension subspaces. The OBSAR based on oblique projection [6] consists of projecting the received signal into the target subspace along the interference one. Compared to the SSDSAR, the oblique projection allows us to reduce random noise and the interferences at the same time. In addition, the MMT response is not reduced compared to the SISDSAR. We compute and compare the performances of the OBSAR and of the SSDSAR; as the SISDSAR can perform poorly for some interference subspace, its performances are not presented here. We also study the robustness of the OBSAR to interference modeling errors. Finally, we present results on real data from ONERA (the French Aerospace Lab).

The paper is organized as follows: Section 2 describes first the SAR configuration and then the MMT and interferences modeling, Section 3 presents the OBSAR algorithm and its performances are computed in Section 4. Section 5 gives the different simulation results and images from real data are presented in Section 6.

## 2. PROBLEM STATEMENT

### 2.1. SAR configuration and notations

In SAR configuration, we consider that an antenna evolves along a linear trajectory; at each position  $u_i$ ,  $i \in \llbracket 1, N \rrbracket$  the antenna emits a signal and receives the response from the scene

The authors thank the DGA for funding this project and the ONERA for providing us real data.

under observation (see figure 1). The distance between adjacent positions is constant and equal to  $\delta u$ . The emitted signal is a chirp in polarization H and V with a frequency bandwidth  $B$ , a central frequency  $f_0$  and a duration  $T_e$ . We denote by  $\mathbf{z}_{pi} \in \mathbb{C}^{K \times 1}$  the received signal samples at every  $u_i$  position of the antenna in polarization  $p$  ( $p=H$  or  $p=V$ ) and  $K$  is the number of time samples. The total received signal  $\mathbf{z}_p$  for one polarization channel is the concatenation of the  $N$  vectors  $\mathbf{z}_{pi}$  [2]:

$$\mathbf{z}_p \in \mathbb{C}^{NK \times 1}, \quad \mathbf{z}_p = [\mathbf{z}_{p1}^T \quad \mathbf{z}_{p2}^T \quad \dots \quad \mathbf{z}_{pN}^T]^T \quad (1)$$

The total polarimetric received signal  $\mathbf{z}$  is then the concatenation of  $\mathbf{z}_H$  and  $\mathbf{z}_V$ :

$$\mathbf{z} \in \mathbb{C}^{2NK \times 1}, \quad \mathbf{z} = [\mathbf{z}_H^T \quad \mathbf{z}_V^T]^T \quad (2)$$

In this paper, we precise that only the co-polarized channels are considered ( $H = HH$  and  $V = VV$ ).

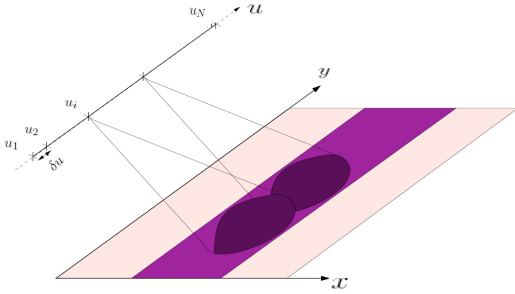


Fig. 1. SAR geometry configuration.

## 2.2. MMT and interferences modeling

For FoPen detection, we consider two kinds of deterministic scatterer: the MMT (signal of interest) and the trunks of the forest (the interferences) which are the main cause of false alarms. We model these scatterers by canonical elements which allow to generate a target and an interference subspaces.

We suppose that a MMT can be seen as a set of perfectly conducting (PC) plates with unknown orientations and whose scattering is computed by using Physical Optics (PO) [7]. Moreover, we assume that for every possible orientations of the plate at the position  $(x, y)$ , its SAR response belongs to a low dimension-subspace  $\langle H_{xy} \rangle$  of rank  $D_H$  [2]. The received signal from a MMT at the position  $(x, y)$  is then written as:

$$\mathbf{z} = \mathbf{H}_{xy} \boldsymbol{\lambda}_{xy} \quad (3)$$

where  $\mathbf{H}_{xy} \in \mathbb{C}^{2NK \times D_H}$  is an orthonormal basis of the target subspace  $\langle H_{xy} \rangle$  and  $\boldsymbol{\lambda}_{xy} \in \mathbb{C}^{D_H \times 1}$  is an unknown coordinate vector of  $\mathbf{z}$  in the target subspace.

We assume that a trunk is modeled by a dielectric cylinder with unknown orientations lying over a PC ground and whose scattering is computed by using the Infinite Cylinder approximation (IC) [7]. As for the target model, we suppose that for each possible orientations of the cylinder at the position  $(x, y)$ ,

its SAR response belongs to a low rank subspace  $\langle J_{xy} \rangle$  of rank  $D_J$  [4]. The received signal from a trunk at the position  $(x, y)$  is then written as:

$$\mathbf{z} = \mathbf{J}_{xy} \boldsymbol{\mu}_{xy} \quad (4)$$

where  $\mathbf{J}_{xy} \in \mathbb{C}^{2NK \times D_J}$  is an orthonormal basis of the interference subspace  $\langle J_{xy} \rangle$  and  $\boldsymbol{\mu}_{xy} \in \mathbb{C}^{D_J \times 1}$  is an unknown coordinate vector of  $\mathbf{z}$  in the interference subspace.

The generation of the subspaces is not described in this paper and details can be found in [2] for the generation of the target subspace at VV polarization. Polarimetric target subspaces (HH and VV) are studied in [3]. Finally, the interference subspace generation is given in [4].

## 3. NEW SAR ALGORITHMS

### 3.1. SSDSAR

The SSDSAR algorithm developed in [2, 3] only uses the target subspace. We consider a MMT located at the position  $(x, y)$  whose scattering is modeled as in Eq. (3) and corrupted by  $\mathbf{n} \in \mathbb{C}^{2NK \times 1}$  which is a zero mean complex Gaussian noise vector with known variance  $\sigma^2$ . The intensity of the SSDSAR image for the pixel  $(x, y)$  has been shown to be:

$$I_{SSD}(x, y) = \frac{\|\hat{\boldsymbol{\lambda}}_{xy}^{SSD}\|^2}{\sigma^2} = \frac{\|\mathbf{H}_{xy}^\dagger \mathbf{z}\|^2}{\sigma^2} \quad (5)$$

We can easily demonstrate that the intensity of the pixel  $(x, y)$  of the SSDSAR image is the orthogonal projection of  $\mathbf{z}$  into  $\langle H_{xy} \rangle$ .

### 3.2. OBSAR

The OBSAR algorithm [5] uses the target and the interference subspaces. We consider a MMT located at the position  $(x, y)$  whose scattering is modeled as in Eq. (3); its response is corrupted by  $\mathbf{n}$  and the signal of a trunk whose scattering is modeled as in Eq. (4). The received signal is then written as:

$$\mathbf{z} = \mathbf{H}_{xy} \boldsymbol{\lambda}_{xy} + \mathbf{J}_{xy} \boldsymbol{\mu}_{xy} + \mathbf{n} \quad (6)$$

The unknown vector  $\boldsymbol{\lambda}_{xy}$  is estimated by using least square method [6]:

$$\begin{aligned} \hat{\boldsymbol{\lambda}}_{xy}^{OB} &= \arg \left( \min_{\boldsymbol{\lambda}_{xy}, \boldsymbol{\mu}_{xy}} \|\mathbf{z} - \mathbf{H}_{xy} \boldsymbol{\lambda}_{xy} - \mathbf{J}_{xy} \boldsymbol{\mu}_{xy}\|^2 \right) \\ &= \mathbf{H}_{xy}^\dagger \mathbf{E}_{\mathbf{H}_{xy} \mathbf{J}_{xy}} \mathbf{z} \end{aligned} \quad (7)$$

where  $\mathbf{E}_{\mathbf{H}_{xy} \mathbf{J}_{xy}}$  is the oblique projector into  $\langle H_{xy} \rangle$  along  $\langle J_{xy} \rangle$ . The intensity of the OBSAR image for the pixel  $(x, y)$  is then defined as follows:

$$I_{OB}(x, y) = \frac{\|\hat{\boldsymbol{\lambda}}_{xy}^{OB}\|^2}{\sigma^2} = \frac{\|\mathbf{H}_{xy}^\dagger \mathbf{E}_{\mathbf{H}_{xy} \mathbf{J}_{xy}} \mathbf{z}\|^2}{\sigma^2} \quad (8)$$

Compared to the SSDSAR image, the intensity of the OBSAR image depends on the oblique projection of the received signal  $\mathbf{z}$  onto the target subspace along the interference one.

In terms of target detection, the SSDSAR and the OBSAR are developed to increase the MMT response embedded in random noise. Concerning false alarms due to the trunks, the SSDSAR and the OBSAR give different results. In the SSDSAR image, the trunks have non-null responses while the OBSAR is made to suppress them.

#### 4. STATISTICAL PERFORMANCES OF THE SSDSAR AND THE OBSAR

In this section, we evaluate the statistical performances of the OBSAR and we compare them to those of the SSDSAR. In real environment, it is difficult to perfectly know the origin of false alarms. For FoPen detection, false alarms are mainly due to the trunks but branches and foliage of trees may also cause false alarms. We then consider two cases for the interferences: the ideal one in which the interference response totally lies in the interference subspace and the realistic case in which a part of the interference response does not lie in the interference subspace. As we know that the target is a MMT, we assume that its response totally belongs to the target subspace.

##### 4.1. Probability of detection

Let us assume that only a MMT is located at the position  $(x_1, y_1)$ . For a given threshold  $\eta$ , the probabilities of detection for the SSDSAR and the OBSAR are defined by  $P_d = P(I_{SSD}(x_1, y_1) > \eta)$  and by  $P_d = P(I_{OB}(x_1, y_1) > \eta)$ . We derive then the distribution of each algorithm. From Eq. (5), the distribution of the SSDSAR is [8]:

$$I_{SSD}(x_1, y_1) \sim \frac{1}{2} \chi^2 \left( 2D_H, 2 \frac{\|\hat{\lambda}_{x_1 y_1}^{SSD}\|^2}{\sigma^2} \right) \quad (9)$$

where  $\chi^2(a, b)$  is the non-central  $\chi^2$  distribution with a dimension  $a$  and a non-central parameter  $b$ . From Eq. (8), the distribution of the OBSAR is [8]:

$$I_{OB}(x_1, y_1) \sim \frac{1}{2} \chi^2 \left( 2D_H, 2 \frac{\|\hat{\lambda}_{x_1 y_1}^{OB}\|^2}{\sigma^2} \right) \quad (10)$$

##### 4.2. Probability of false alarm $P_{fa}$

We consider now that an interference is located at the position  $(x_0, y_0)$ . The probabilities of false alarms for the two algorithms are defined by  $P_{fa} = P(I_{SSD}(x_0, y_0) > \eta)$  and by  $P_{fa} = P(I_{OB}(x_0, y_0) > \eta)$ .

###### • Ideal case

We suppose that the interference scattering totally lies in  $\langle J_{x_0 y_0} \rangle$  as illustrated in Fig. 2(a). From Eq. (5), the distribution of the SSDSAR then becomes:

$$I_{SSD}(x_0, y_0) \sim \frac{1}{2} \chi^2 \left( 2D_J, 2 \frac{\|\mathbf{H}_{x_0 y_0}^\dagger \mathbf{J}_{x_0 y_0} \boldsymbol{\mu}_{x_0 y_0}\|^2}{\sigma^2} \right) \quad (11)$$

If the two subspaces are orthogonal, the  $P_{fa}$  for the SSDSAR will not depend on the interference response. However, the target and interference subspaces are generally not orthogonal which involves a dependence of this  $P_{fa}$  to the relative position of the target and the interference subspaces.

From Eq. (8), the distribution of the OBSAR is:

$$I_{OB}(x_0, y_0) = 0 \sim \frac{1}{2} \chi^2 \left( 2D_J, 0 \right) \quad (12)$$

As the interferences are totally removed by the oblique projection, the  $P_{fa}$  for the OBSAR does not depend any more on the interference response.

###### • Realistic case

We suppose now that a part of the interference scattering  $\boldsymbol{\delta}_{x_0 y_0}^J$  does not belong to  $\langle J_{x_0 y_0} \rangle$  as illustrated in Fig. 2(b). Therefore, we get the following received signal:

$$\begin{aligned} \mathbf{z} &= \mathbf{J}_{x_0 y_0} \boldsymbol{\mu}_{x_0 y_0} + \boldsymbol{\delta}_{x_0 y_0}^J + \mathbf{n}, \\ \mathbf{z} &\sim \mathcal{N}(\mathbf{J}_{x_0 y_0} \boldsymbol{\mu}_{x_0 y_0} + \boldsymbol{\delta}_{x_0 y_0}^J, \sigma^2) \end{aligned} \quad (13)$$

where  $\mathcal{N}(a, b)$  is the normal distribution of mean  $a$  and variance  $b$ . From Eq. (5), the distribution of the SSDSAR then becomes:

$$I_{SSD}(x_0, y_0) \sim \frac{1}{2} \chi^2 \left( 2D_J, 2 \frac{\|\mathbf{H}_{x_0 y_0}^\dagger (\mathbf{J}_{x_0 y_0} \boldsymbol{\mu}_{x_0 y_0} + \boldsymbol{\delta}_{x_0 y_0}^J)\|^2}{\sigma^2} \right) \quad (14)$$

From Eq. (8), the distribution of the OBSAR is:

$$I_{OB}(x_0, y_0) \sim \frac{1}{2} \chi^2 \left( 2D_J, 2 \frac{\|\mathbf{H}_{x_0 y_0}^\dagger \mathbf{E}_{\mathbf{H}_{x_0 y_0} \mathbf{J}_{x_0 y_0}} \boldsymbol{\delta}_{x_0 y_0}^J\|^2}{\sigma^2} \right) \quad (15)$$

Compared to the ideal case, the  $P_{fa}$  for the OBSAR depends on the part of the interference response not described by the interference subspace. Nevertheless, we expect that the OBSAR gives better performances compared to the SSDSAR in the *realistic case*; indeed as shown in Fig. 2(b), the oblique projection of the interference response into the target subspace is lower than the orthogonal one.

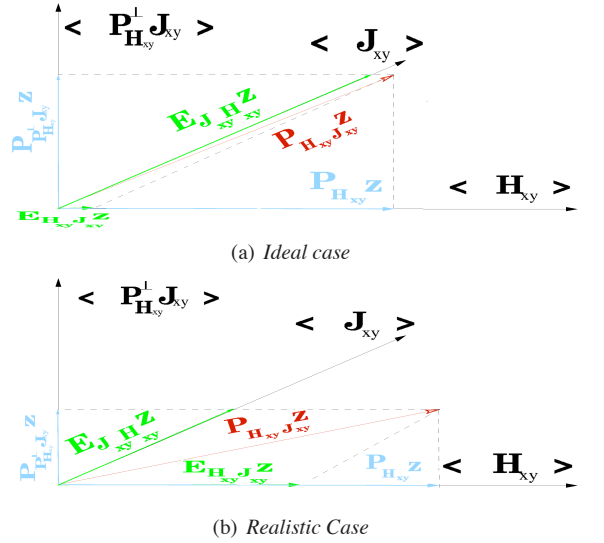


**Fig. 2.** Interference projections for the ideal (Top) and the realistic (Bottom) cases.

## 5. SIMULATION RESULTS

### 5.1. Configuration

We consider a flight between the first position  $u_1 = -50m$  and the last position  $u_{200} = 50m$  with  $\delta_u = 0.5m$  between each position and an altitude of  $100m$ . The full polarized emitted signal is a chirp with  $f_0 = 400MHz$ ,  $B = 100MHz$  and  $T_e = 2.10^{-7}s$ . The radar scene is defined in  $[90, 140]m$  for range axis (x) and  $[-25, 20]m$  for azimuth axis (y).

To generate the bases  $\mathbf{H}_{xy}$  and  $\mathbf{J}_{xy}$ , we choose a PC plate of size of  $2m \times 1m$  for the model of the target and a dielectric cylinder of height of  $11m$  and of radius of  $20cm$  lying over a ground for the model of the interference. The subspaces  $\langle H_{xy} \rangle$  and  $\langle J_{xy} \rangle$  have the same rank 10 [2].

The MMT is a PC box with size  $2m \times 1.5m \times 1m$  lying over a PC ground whose scattering is simulated with FEKO [9]. For the *ideal case*, the interference is a dielectric cylinder over a PC ground as for the interference subspace generation. For the *realistic case*, the interferences are trunks over dielectric ground simulated with COSMO [10] which is a software dedicated to the realistic simulation of forest scattering. Compared to the ideal case, the ground here is not PC and the attenuation due to the foliage of the forest canopy is taken into account. In both cases, the Signal to Interference Ratio is equal to  $-10dB$ . A very high Signal to White Noise Ratio of  $35dB$  is chosen in order to study especially the contribution of the interferences in the performances and the robustness of both algorithms.

Classical SAR algorithms results on these simulated data are not presented here. In the classical SAR images, the target response is very low and the trunks ones are very high. These images can be found in [2].

## 5.2. Receiver Operating Characteristics (ROC)

To evaluate the performances of the SSDSAR and the OBSAR, the ROC,  $P_d$  versus  $P_{fa}$ , are plotted in Fig. 3(a) for the *ideal case* and in Fig. 3(b) for the *realistic case*. For the *ideal case*, we reach a  $P_d$  higher than 0.9 for a  $P_{fa}$  higher than  $10^{-5}$  in the OBSAR and a  $P_{fa}$  higher than  $7.10^{-2}$  in the SSDSAR. First, poor performances of the SSDSAR compared to the performances of the OBSAR show that the target and the interference subspaces are not orthogonal. Therefore, the oblique projection of the OBSAR algorithm is needed for a complete removal of the interferences and for obtaining great performances. For the *realistic case*, we reach a  $P_d$  higher than 0.9 for a  $P_{fa}$  higher than 0.3 in the OBSAR and a  $P_{fa}$  higher than 0.7 in the SSDSAR. Performances of the SSDSAR and the OBSAR are degraded compared to those obtained in the ideal case. This is explained by the foliage attenuation and the dielectric ground which are not taken into account in the interference subspace. However, the OBSAR still outperforms the SSDSAR which shows the interest of the oblique projection.

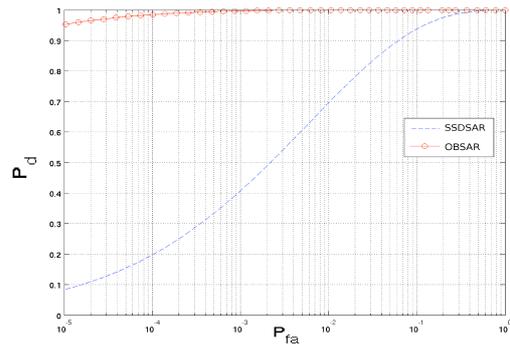
## 5.3. Images

The images obtained by the SSDSAR and the OBSAR in the realistic case are shown in Fig. 4(a) and Fig. 4(b). In both images, the target pixel has the highest intensity. In the SSDSAR image, we have a difference of  $1.5dB$  between the target intensity and the maximum of the interference intensities. This result becomes  $3dB$  in the OBSAR image. Therefore, the OBSAR leads to a reduction of false alarms compared to the SSDSAR.

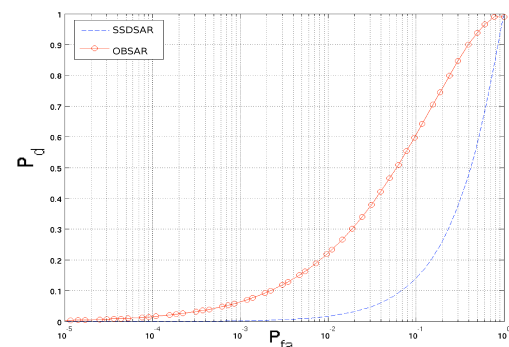
## 6. REAL DATA IMAGES

### 6.1. Configuration

The real SAR data presented in this section have been acquired during the PYLA'2004 campaign (Landes, France), us-



(a) Ideal case



(b) Realistic Case

**Fig. 3.** ROC plots for the SSDSAR and the OBSAR in the ideal case (Top) and realistic (Bottom) cases.

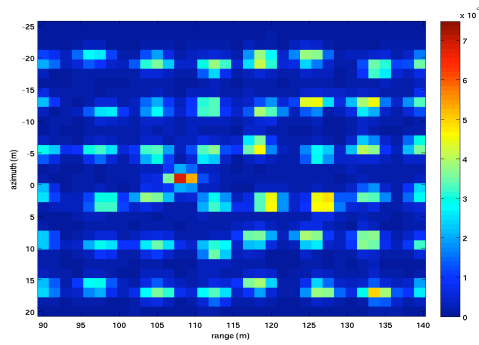
ing the SAR system RAMSES from ONERA at frequencies between  $400MHz$  and  $470MHz$  and with an incidence angle of  $59.8^\circ$ . For more details on the Nezer forest, see [10]. The target is a truck with an orientation parallel to the radar flight and placed in the forest of pines.

To generate the bases  $\mathbf{H}_{xy}$  and  $\mathbf{J}_{xy}$ , we choose a PC plate of size of  $4m \times 2m$  for the model of the target and a dielectric cylinder of height of  $11m$  and of radius of  $20cm$  lying over a PC ground for the model of the interference. The subspaces  $\langle H_{xy} \rangle$  and  $\langle J_{xy} \rangle$  have the same rank 10.

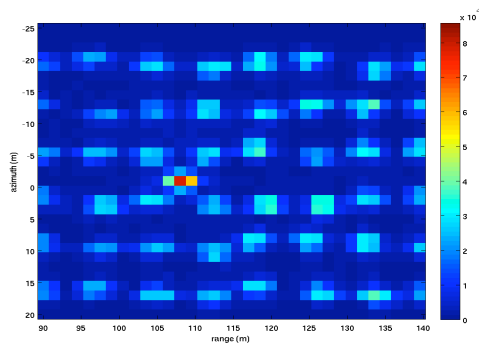
As for the simulated data, the classical SAR images are not presented here and can be found in [2]: the truck is not visible and the forest causes many false alarms.

### 6.2. Images

We present the images given by the SSDSAR in Fig. 5(a) and by the OBSAR in Fig. 5(b). First, we clearly distinguish the truck from the environment in the SSDSAR and the OBSAR images. Secondly, we see that the background intensity is slightly reduced in the OBSAR image. More precisely, we have a difference of  $1.7dB$  between the target intensity and the maximum of the interference intensities in the SSDSAR and a difference of  $2.3dB$  for the OBSAR image. The OBSAR shows then better performances than the SSDSAR in terms of false alarms reduction.



(a) SSDSAR



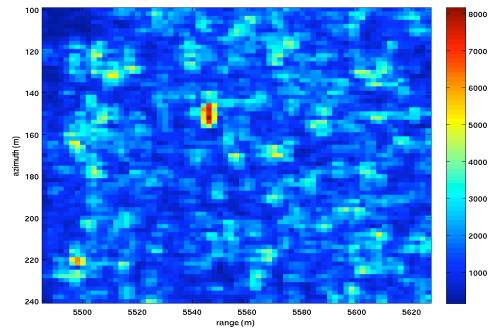
(b) OBSAR

**Fig. 4.** SSDSAR and OBSAR images for realistic simulated data. A box over the ground located at  $(108, -1, 0)m$  is placed in a forest of trunks.

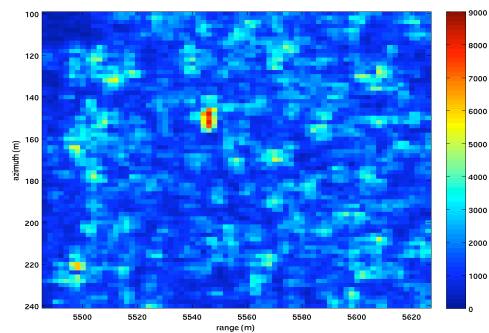
Finally, these results show the robustness of our algorithms to the target modeling. As discussed in section 4.2, the performances of the OBSAR depend on the modeling errors on the interferences. So, we expect to have a limited reduction of the false alarms. Nevertheless, we observe in Fig. 5(b) that the OBSAR still outperforms the SSDSAR.

## 7. CONCLUSION

We proposed a new SAR processor for FoPen application, denoted by OBSAR, based on oblique projection in order to improve target detection and to reject interferences. We computed the statistical performances of the OBSAR and compared them to those of the SSDSAR (developed in a previous work): the OBSAR outperforms the SSDSAR. In order to use the OBSAR in realistic cases, we also studied its robustness to interference modeling errors. Even if the performances are then degraded, false alarms due to the interferences are reduced. Finally, we confirmed these results on real data. For future work, it is needed to improve the interference modeling to obtain better false alarm reduction. For example, principal branches responses and foliage attenuation effects could be included in our interferences model. It would also be interesting to use cross-polarized channels in order to improve target detection and false alarms reduction.



(a) SSDSAR



(b) OBSAR

**Fig. 5.** SSDSAR and OBSAR images for real data. A truck located at  $(5550, 150, 0)m$  is placed in the Nezer forest.

## 8. REFERENCES

- [1] M. Soumekh, *Synthetic Aperture Radar Signal Processing*, Wiley - Interscience Publication, 1999.
- [2] R. Durand, G. Ginolhac, L. Thirion-Lefevre, and P. Forster, "New SAR processor based on matched subspace detectors," *IEEE Trans. on Aerosp. and Electron. Syst.*, vol. 45, no. 1, pp. 221 – 236, January 2009.
- [3] F. Brigui, L. Thirion-Lefevre, G. Ginolhac, and P. Forster, "New polarimetric signal subspace detectors for SAR processors," *CR. Acad. Sci. IV*, vol. 11, no. 1, pp. 104 – 113, January 2010, Propagation and remote sensing.
- [4] G. Ginolhac, L. Thirion-Lefevre, R. Durand, and P. Forster, "SAR processors based on signal or interference subspace detector," *IEEE Trans. on Aerosp. and Electron. Syst.*, vol. 46, no. 3, pp. 1006 – 1020, July 2010.
- [5] F. Brigui, G. Ginolhac, L. Thirion-Lefevre, and P. Forster, "Oblique polarimetric SAR processor based on signal and interference subspace models," in *IGARSS 10, Honolulu, Hawaii, USA*, July 2010.
- [6] R.T. Behrens and L.L. Scharf, "Signal processing applications of oblique projection operators," *IEEE Trans. on Signal Process.*, vol. 42, no. 6, pp. 1413 – 2124, June 1994.
- [7] F.T. Ulaby and C. Elachi, *Radar Polarimetry for Geoscience Application*, F.T. Ulaby, C. Elachi Editors, 1990.
- [8] L.L. Scharf, *Statistical Signal Processing: Detection, Estimation and Time Series Analysis*, Addison-Wesley Publishing Co., 1990.
- [9] *Feko, User's Manual, EM Software and System*, 2004.
- [10] L. Thirion, E. Colin, and C. Dahon, "Capabilities of a forest coherent scattering model applied to radiometry, interferometry and polarimetry at p and l bands," *IEEE Trans. on Geosci. and Remote Sens.*, vol. 44, no. 4, pp. 849 – 862, April 2006.